Texture and microstructure characterizations of Fe-3.5wt%Si soft magnetic alloy fabricated via laser powder bed fusion

Xiaojun Shen[a*], Fanbo Meng[a], Kwang Boon Lau[b], Pei Wang[b,c], Christopher H. T. Lee[a*]

[a]*School of Electrical and Electronic Engineering, Nanyang Technological University, 50 Nanyang Avenue, 639798, Singapore.*

[b]*Institute of Materials Research and Engineering, Agency for Science, Technology and Research, 138634, Singapore*

[c]*Engineering Cluster, Singapore Institute of Technology, 519961, Singapore*

[*]*Corresponding author email address:*

~~s673864902@126.com~~

chtlee@ntu.edu.sg

Formatted: Superscript

Commented [CHTL(P1]: I just confirmed with the sponsor and they said only PI can be the corresponding author.

Abstract

Manufacturing stable grain-oriented electric steel with fewer procedures remains a challenge due to the formation of detrimental γ-fiber//ND texture. In this work, Laser Powder Bed Fusion (LPBF) process was employed to obtain a strong λ-fiber (//ND) texture in a Fe-3.5wt%Si electrical steel. The texture and microstructure were characterized by Electron Backscatter Diffraction (EBSD), Scanning Electron Microscopy/Energy Dispersive X-ray Spectroscopy (SEM/EDS) and High-Resolution Transmission Electron Microscopy (HRTEM). The EBSD results showed a strong λ-fiber texture on the top plane of Fe-Si alloy. It included {001}<001> Cube texture, {001}<110> rotated cube texture and {100}<105> texture. With the low energy density, an area fraction of 16% γ-fiber texture was formed on the top plane. Additionally, the formation of amorphous precipitates in additively manufactured Fe-Si alloy was firstly reported. The lattice constant of 2.7975Å was calculated in the matrix area. The work has shown LPBF can open a new door to manufacture grain-oriented electrical steel for industrial applications.

Keywords: Additive manufacturing; Laser bed powder fusion; Microstructure; Amorphous precipitates; Texture;

1. Introduction

Electrical motors have greatly piqued the interest of researchers all around the world, because of rapid growth of the electric vehicle market and ever-higher efficiency criteria. Currently, electric motors are primarily designed with lamination structure of silicon steel, benefitted from their economical cost, outstanding magnetic performance, and adequate mechanical strength. Since its invention in 1880s, Fe-Si alloys have still been the main material to produce laminated cores for electrical equipment [1]. Fe-Si alloys can be categorized into two major groups, namely non-oriented electrical steel (NOES) and grain-oriented electrical steel (GOES), with doping varied silicon content to meet the needs of diverse applications. The GOES with Goss texture ({110}<001>) exhibits outstanding magnetic performance of low core losses and strong magnetic induction parallel to the rolling direction. Therefore, the GOES have

been widely employed as the transformer core. But this is not the case in the transverse direction, where the optimal GOES for a rotating magnetic field is not available. Although NOES is referred to "non-oriented" in comparison to GOES, it is magnetized to all directions of the laminated plane in the motor core, i.e., the easy magnetization <100> axes lie in the sheet plane and a <100>//ND texture is needed. Cube texture ({100}<001>) contains two easy magnetization directions, i.e., lie in the transverse and rolling direction, to optimize the efficiency of electric motors. The NOES are manufactured with several procedures, such as purification, hot rolling, pickling, cold rolling annealing, temper rolling and insulation coating [2]. However, these conventional manufacturing processes are difficult to create cube texture, because cube orientation is unstable and tends to transform into γ and α-fiber texture in the final products [3].

Numerous innovative trials have been made to investigate the formation of electrical steels with strong {100} texture or cube texture. Cross rolling and subsequent annealing lead to a secondary recrystallization of cube texture in NOES by Taguchi *et al.* [4]. Tomida *et al.*, [5] acquired {001} texture in NOES using the transformation of γ→ α phases by the decarburization under a vacuum. Liu *et al.*,[6] developed columnar grains with λ-fiber (<001>//ND) texture using twin-roll strip casting technique, followed by cold rolling and annealing in 3.2wt%Si-0.7wt%Al NOES. Fang *et al.*, [7] reported a phenomenon with remarkable abnormal grain growth of {100} grains appearing in the as-casted strip after annealing. Grain size advantage and surface energy is attributed to the formation of abnormal grain growth of {100} grains in NOES. Unlike the conventional rolling and annealing routes, Mehdi *et al.*, [8] proposed to alter the initial texture by a simple rolling scheme before cold rolling. Such pre-engineering process resulted a rotated Goss texture that would produce cube crystallites after rolling process within the shear bands where nucleated a strong cube texture in the final sheet. Zhou *et al*., [9] acquired a strong cube texture with orientation distribution function (ODF) density of 50.73 mrd using cross-rolling and pulsed electric current technique in the grain-oriented electric steel.

Apart from the above techniques, Laser Powder Bed Fusion, is another promising way to induce crystallographic textures [10]. With its characteristics of computer-aided-design, the conventional lamination structure of electric motors could be integrated into an integrated structure without multiple conventional processes such as cutting, punching and coating insulating layers. Recent investigations showed that Fe-Si alloys can be successfully printed using additively manufacturing techniques. A near-full density high-silicon steel (Fe-6.9wt%Si) was successfully fabricated with LPBF by Garibaldi *et al.* [10]. They reported a <001> fibre-texture along the build direction, which transforms into a cube texture when the laser energy increases. They also found that the annealed sample can still retain the crystallographic orientation induced by as-printing process [11]. Goll *et al.* developed large columnar grains along building direction in Fe-6.5wt%Si alloy [12]. It was found that scan pattern and geometry also have a critical influence on the microstructure of Fe-Si alloy during the LPBF process. Both single and double scanning strategy have induced fibre texture (<100> type) on the normal (XY) and parallel (XZ) planes, while the double scanning strategy exhibited stronger texture intensity in comparison to single scanning. Additionally, Plotkowski *et al.*, [13] designed and fabricated a Hilbert-curve inspired Fe-3wt%Si and Fe-6wt%Si transformer core via laser powder bed fusion. The magnetic performance showed the AM transformer have comparable or even better performance in comparison to NOES sheet. However, the core losses are higher than the GOES sheet. Although the grain size increased dramatically after annealing, the γ-fibre or near γ-fibre texture were also formed in both IPF maps of the annealed

3wt%Si and 6wt%Si sample. In the electric motor area, Koo *et al.*, [14] also designed and printed structurally-layered stators (Fe-6.5wt%Si alloy) for novel axial-flux motors using LBPF and surface insulation (SiO_2 layer) After heat treatment, the Fe-Si sample exhibits enhanced magnetic performance, i.e. 34.6A/m H_c, 7393 $\mu_{r\,max}$, and 1.68T M_s. However, it is insufficient to analyse the microstructure and texture of the as-printed or the as-annealed Fe-Si sample. And the microstructural analysis of additively manufactured Fe-Si alloys is still far away from complete.

Therefore, in this work, a LPBF machine was employed to print Fe-Si electrical steel bulks, followed by microstructural characterizations using SEM-EDS, EBSD and HR-TEM techniques. An extremely strong λ-fibre texture was successfully produced in the additively manufactured Fe-Si alloy via LPBF. The purpose of this study is to create strong λ-fibre texture for the fabrication of components of transverse flux electric motors as the flux inside the motor is three-dimensional, which might optimize magnetic route and increase power density while maintaining high efficiency.

2. Material characterization and experimental procedures

The atomized Fe-3.5wt%Si (supplier: Coatec, Ltd Singapore) with particle size distribution of D_{10}=15.62μm, D_{50}=27.29μm, D_{90}=46.93μm, shows the uniform spherical morphology in Fig. 1b. The nominal chemical composition of the Fe-3.5wt%Si powder is: 3.44wt% Si, 0.052 wt% O, 0.006wt% C, 0.009 wt% P, 0.003wt% S and balanced Fe.

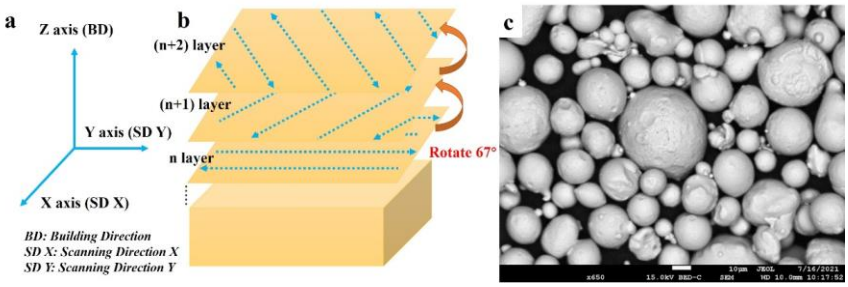

Fig. 1 The schematic diagram of the sample coordinate (a), laser scanning strategy (b) and the BSE image of 3.5Si Spherical powders(c)

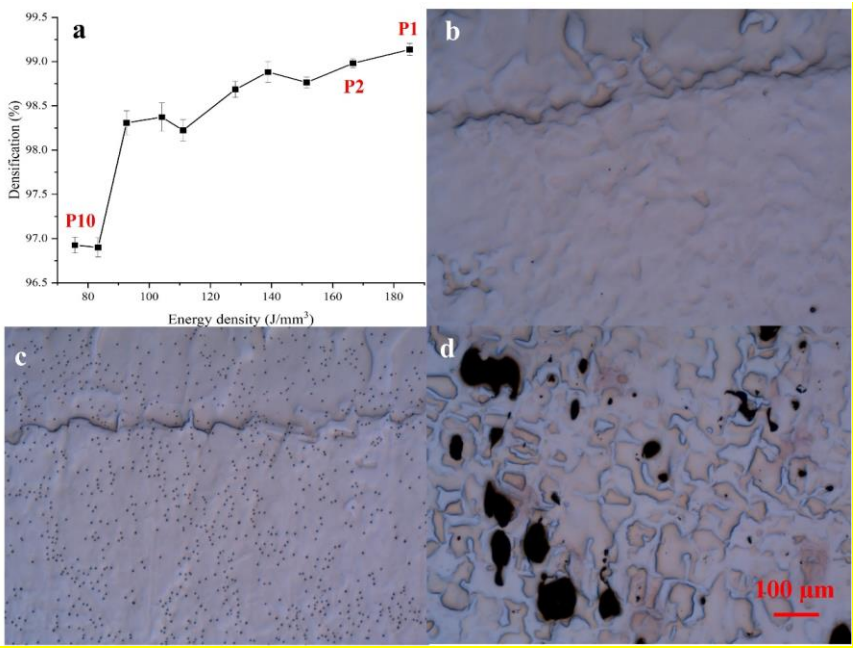

Fig. 2 Densification curves(a); Optical Microscope image for Parameter 1(b); OM image for the top-view of Parameter 2 (c) ;OM image for the top-view of Parameter 10 (d)

Table 1 The detailed parameters of laser powder bed fusion process

Laser Power (W)	Layer thickness(μm)	Hatch spacing(μm)	Rotate angle (°)	Speed (mm/s)	Energy density (J/mm^3)	Nomination
150	20	90	67	1100	75.76	P10
				1000	83.33	N.A.
				900	92.59	
				800	104.17	
				750	111.11	
				650	128.21	
				600	138.89	
				550	151.52	
				500	167	P2

	450	185	P1

The 3D printing work was carried out using TruPrint 1000 manufactured by Trumpf ptd Ltd., equipped with a 200w Yb-YAG fibre laser with a focal diameter of 30µm. The powders were deposited onto a steel substrate with a diameter of 100mm. Argon gas (purity: 99.999%) was used to reduce the content of oxygen to around 100 ppm to avoid any oxidation happened during the printing process. As shown in Fig. 1~~Fig. 1~~a. ~~A~~the stainless steel plate without preheating was employed as substrate to support the printing work. The strips scanning strategy with a rotation angle of 67° by layers was employed to reduce the internal residual stress and thermal effects~~, as shown in Fig. 1a~~. More detailed LPBF parameters with corresponding nomination can be found in Table 1. The density measurement of the printed samples was carried out using Archimede`s Principle with XSE204 Analytical Balance, Mettler-Toledo ltd., Swiss. All the samples in this work were in as-built condition without any heat treatment.

The microstructure of additively manufactured Fe-3.5wt% Si alloy was characterized by SEM/EDS, EBSD and TEM techniques. The as-received bulk sample with a dimension of 5 by 5 by 5 mm was cut into sample pieces, followed by the procedures of grinding using silicon carbide papers and polished with 9µm, 3µm, OPS polishing suspensions to the mirror-like surface. The EBSD detector (symmetry, Oxford instrument, UK) was equipped on a Field Emission Scanning Electron Microscopy (FESM, JEOL Model 7800, Japan). The texture was characterized by ODF and the deviation angle for texture component is 20°. The TEM sample was prepared with FIB (Focusing Ion Beam) on a Zeiss SEM 550 Model using various currents (30nA, 3nA, 300pA, 50pA and low kV polishing). A JEOL 2100F electron microscope was used for TEM/HRTEM observation.

3. Results

3.1 Textural characterization

As contrast, Fig. 3 illustrate the crystallographic orientations of the as-received 3.5Si powder. From the pole figure (Fig. 3b), it can be seen that the orientation of grains distributed randomly and the maximum m.u.d is 10.88. The large angle (>10°) grain boundary is indicated by black lines while the low angle (2°~10°) boundary is shown by grey lines. There are more than 2 grains with different orientations inside one powders and the subgrain boundary can also be found inside the grains. This is because nucleareation in a coarser particle nucleartion can occure at a greater number of places than those in a finer particle. Furthermore, the latent heat and re-solidifcation ~~caused remlting is~~are more likely to cause remelting~~happen~~ in coarser particles, and hence ~~which~~ leading ~~to~~ the coarse particles to have multiple fine grains. [15]

There are many works showing 3D printed microstructure could exhibit strong crystal textures with <001> orientation parallel to the build direction [16-19]. In this work, a strong {001}//BD (λ-fiber) texture is obtained in all three samples along Z direction, as seen in Fig. 4. The <001> crystal orientations of the as-built sample (P1&P2) are nicely aligned with the building direction. As previously stated, there are several beneficial texture components (e.g., {001}<001> Cube texture, {001}<110> rotated cube texture and {110}<001> goss texture) in the electrical steels. In Fig. 4a, the IPF Z map of the P1 top plane (X&Y plane) showed that almost all grains are aligned along the ND direction. The responding texture mapping (Fig. 4b) of P1 top showed that there are no {110}<001> texture and {111}//BD. The largest composition part is {001}<110> texture (40.1%), followed by {001}(105) texture (30.9%) and {001}<001> Cube

texture (19.1%). Additionally, there are limited grains whose axis is along with <110> direction as indicated by green color. As reported by S.Takajo *et al.* [3, 20], Rotated Cube texture also exhibited outstanding magnetic properties in the direction of 45° to the rolling direction. However, the formation of Rotated Cube texture is difficult since it is stable during rolling processing, but it is difficult to grow during annealing or is devoured by the growth of other grain orientations like {111}//BD grains. The phenomena come with the fact that the Rotated Cube texture gets less stored energy during the cold rolling processing. Rotated cube was found in a low carbon steel after severe cold rolling at 99.8%, but the 99.8% cold rolled sample also show an abnormally strong a-fiber deformation texture [20]. Sam *et al.*, [21] found that only 5% Rotated Cube texture was obtained after the first heavy cold rolling in Fe-3%Si electric steel. With the annealing processing, it increased to 40% but nearly no changes in the subsequent cold rolling and annealing processing. As shown in Fig. 4, nearly one-third with orientation {001}<105> is formed. Zhou [9] *et al.*, found a specific recrystallization texture rotation path in the cross cold rolling together with electric pulsed treatment, namely: {114}<261> →{114}<151> →{114}<041>→ {001}<150> → {001}<150> →{001}<010>. Additionally, Liu *et al.*, [6] developed λ-fiber texture with a peak at {001}<510> in a non-orientated Fe-3.2wt%Si sheet with cold rolling and annealing. The magnetic induction was greatly strengthened. The favoured nucleation and grain growth via the strain-induced grain boundary migration mechanism result in the formation of {001}<510> texture.

In Fig. 4c and Fig. 4d, the laser scanning paths can be observed sharply. The dominate texture is {001}//BD fiber texture with peaks at {100}<001>, {100}<110> and {100}<105>. The {110}<001> texture (Goss) is nearly not formed on the P2 top plane while the {111}//BD start to emerge with an area fraction of 0.02%. The {111} oriented grains of blue colour are distributed randomly on the P2 top plane as shown in Fig. 4c.

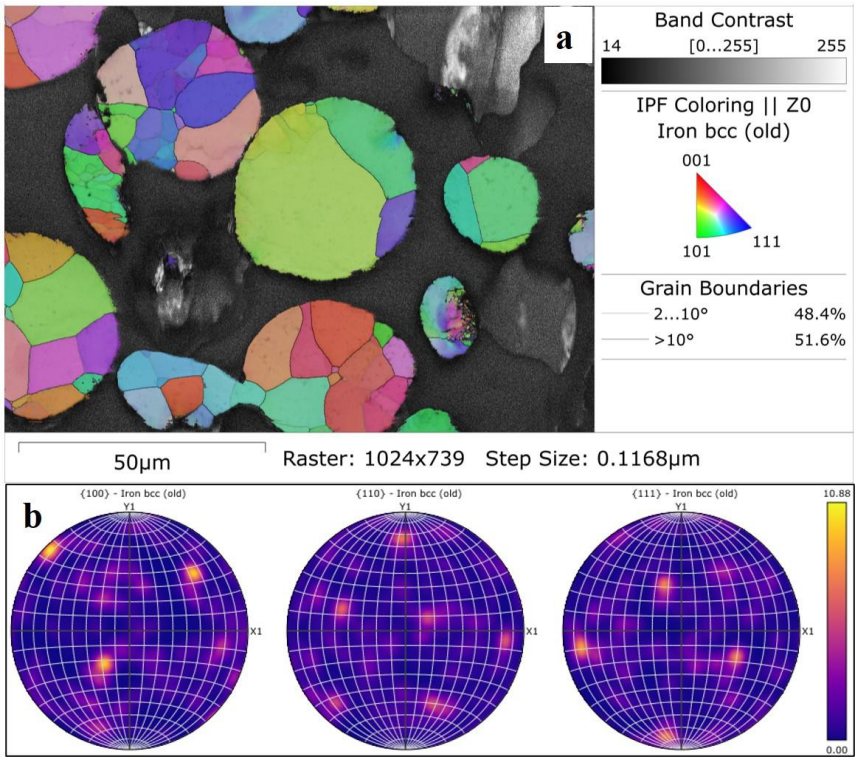

Fig. 3 The IPF EBSD mapping and its corresponding pole figure showing the crystallographic orientations of the as-received Fe-3.5wt%Si powders.

As the energy density of P10 is the lowest among the samples, there are lots of defects such as pores of unmelted particles on the P10 top plane, as seen by the grey background in Fig. 4e. The crystallographic orientation is dominated by {001}//BD texture (including {001}<110> texture, {001}<110> texture and {100}<105> texture), while the {110}<001> texture is extremely weak. It should be noted that the area fraction of {111}//BD fibre texture increases dramatically to 16%, as indicated in blue colour, with much more {111} oriented grains formed on the P10 top plane. Therefore, the laser energy density is proven to be an effective method to regulate the crystal orientations of magnetic components.

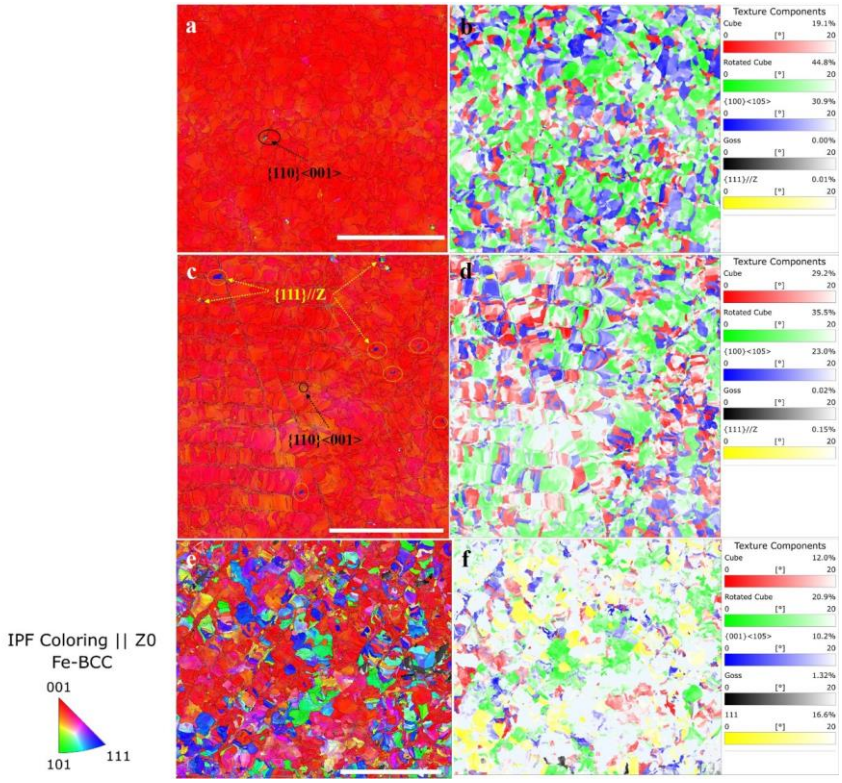

Fig. 4 Inverse pole figure mapping and corresponding texture mapping (20° deviation) of the top-view plane of the additively manufactured Fe-Si alloy: (a)-(b) P1. (c)-(d) P2. (e)-(f) P10. The scale bar is 500 μm

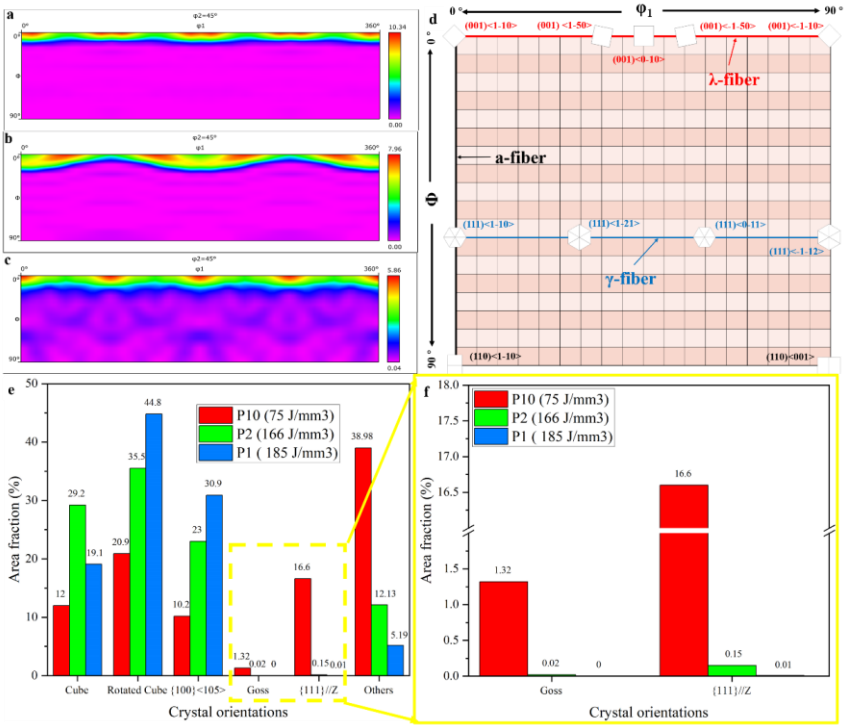

Fig. 5 The texture and area fraction analysis of Fe-Si alloys: (a) ODF mapping of Fe-Si samples. (b) Guide for crystal orientations in φ_2= 45° ODF section. (e) Area fractions of various texture components in the Fe-Si alloys. (f) Magnified mapping for Goss texture and {111} texture.

As shown from Fig. 5a to Fig. 5c, the ODF mappings illustrate the distribution of the crystallographic orientations whose dominated orientation for the P1 to P10 samples is {001}//BD fiber texture. The ODF maximum intensity of {001}//BD fiber texture on the P1 top plane is 10.34 m.u.d, followed by P2 (7.96 m.u.d) and P10 (5.86 m.u.d). In Fig. 5e, it gives out the area fraction of different crystal orientations. The area fraction of rotated cube and {100}<105> texture have a positive correlation with the laser energy density while {111}//BD texture and other textures have a negative one. It should be noted that the area fraction of cube texture does not change with respect to the energy density. In addition, the magnified Fig. 5f illustrates the extreme weak Goss texture on the top plane of the LPBF Fe-Si alloy. The "detrimental" γ-fiber texture is formed on the top plane, when the laser energy density is not high enough, i.e., the optimized laser energy or scanning speed should be chosen to avoid the formation of {111}//BD texture on the top plane.

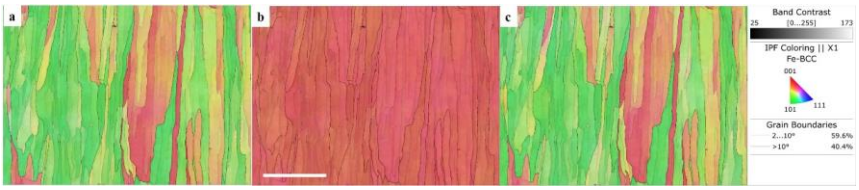

Fig. 6 Cross-scetion EBSD maps: IPF Z (a), IPF Y(b), IPF X(c), the scale bar is 200μm.

Since the conventional EBSD is a 2D surface texture orientation analysis technique, the cross-sectional microstructure should also be evaluated to understand the grain orientation in the additive manufactured bulk sample. Fig. 6 illustrates the IPF mappings of the X&Z plane (P1 sample) from Z (a), Y(b), and X(c) directions. It can be seen that there are {110} and {001} fiber textures in Fig. 6a& Fig. 6c while in Fig. 7b, the grains are all oriented at the <001> direction. Combining with the surface orientation data in Fig. 4a&Fig. 5a and X&Z plane data in Fig. 6, a {001} grain-oriented electrical steel is printed via laser powder bed fusion.

3.2 Microstructural characterization

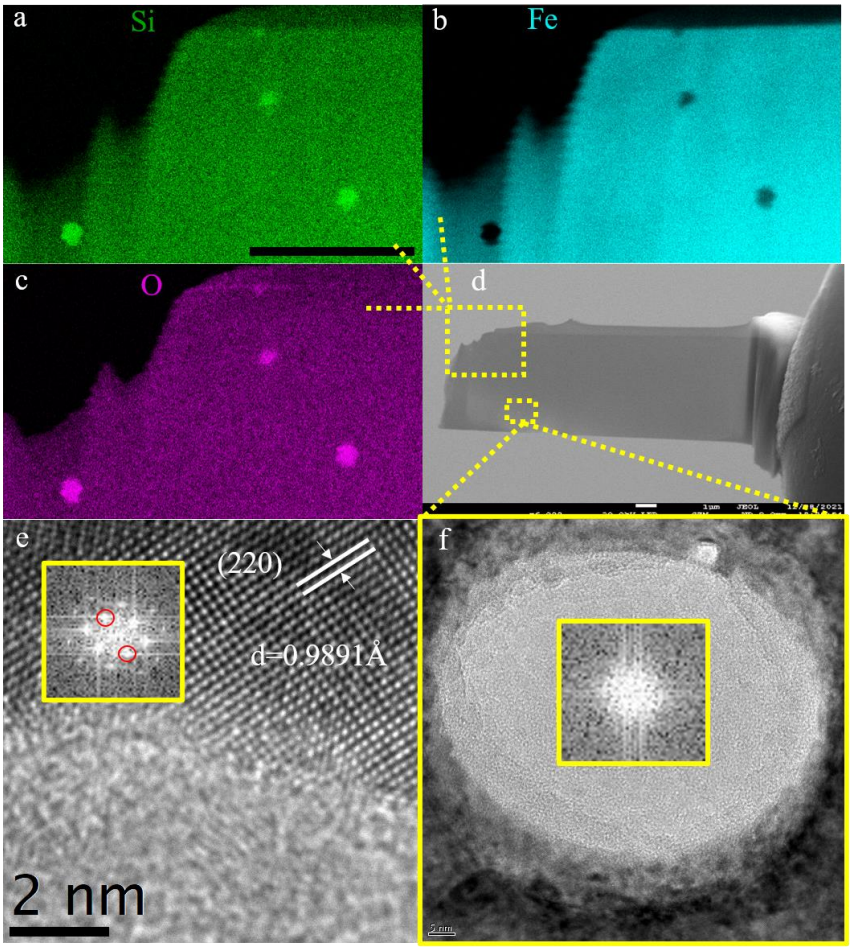

Fig. 7 Amorphous precipitates analysis by TEM and SEM-EDS maps: (a)-(c) SEM-EDS maps showing the elements distributions and enrichment of Si, O in the precipitates. (d) As-prepared sample by FIB technique. (f) TEM image of the amorphous precipitate. (e) Phase contrast of interface between crystal matrix and amorphous precipitate.

In the metallurgical images shown from Fig. 2b to Fig. 2d, the densifications and microstructural defects of Fe-Si samples vary with the energy density. As shown in Fig. 2d (P10, energy density of 87 J/mm^3), there are many defects like pores from unmelted particles with dimension from several microns to hundred microns. By contrast, the Fig. 2b illustrates the top-plane microstructure of the P1 sample, where nearly no defects were seen under the optical microscopy. In order to further investigate the microstructure of LPBF Fe-Si alloy, a FIB sample from the P2 sample, as shown in Fig. 7d, was prepared. Features such as precipitates (as shown in Fig 4f) were found on the FIB sample surface. The dimensions of the features vary from a few nanometers to hundreds of nanometers. The “holes” may be the gas pores

or precipitates formed during the LPBF. Therefore, EDS was employed to analyze the elements distribution on the TEM sample surface. The clear elemental segregation was observed from Fig. 7a to Fig. 7c. Element silicon and oxygen were enriched in the precipitates while element iron is much lower in the precipitates area. In addition, a HRTEM image was taken from the precipitates as shown in Fig 4e. The FFT map of matrix region of interesting is given in Fig. 7e. As highlighted by red circles, the selected pair of diffraction spots is employed to calculate the d spacing (i.e., 0.9891 Å). By matching with PDF card 04-007-9753, the diffraction plane is (220) and the lattice constant was calculated to be 2.7975Å. By contrast, the FFT image of the precipitate in Fig. 7f illustrates that it is amorphous. Therefore, the amorphous precipitates are formed during the LPFB process.

It should be noted there are many small black spots distributed uniformly on the top-plane of the P2 (166J/mm^3) samples. The black spots are pores, while it can be found in the additively manufactured pure Fe from the work of Zafari *et al.*, [22]. The formation of pores is attributed to the lack-of-fusing , i.e., insufficient laser energy density to accomplish optimal melting and solidification conditions during the LPBF processing. In Fig. 8, the SEM-EDS maps shows the area of the black spots are not Si and O enrichment phenomenon. This means the circle-like defects are not precipitates formed during the SLM. It is believed these black spots could be the precursor of the amorphous precipitates, while more tests needed to be carried out to support this guesstimate.

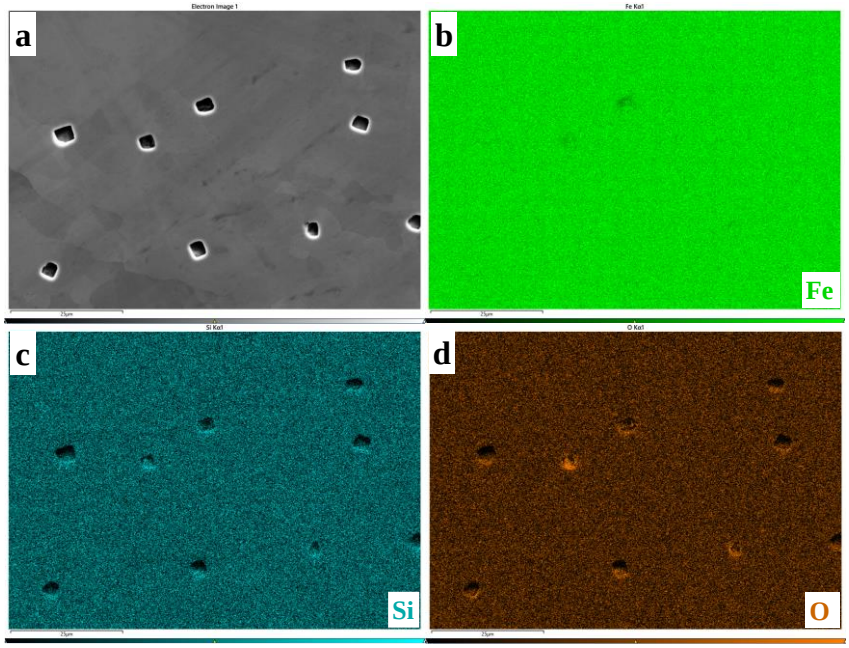

Fig. 8 SEM/EDS images of the P2 sample: (a) SEM image of the P2 sample; (b) to (d) Fe, Si, O EDS maps.

4. Discussion

It is well known that LBPF is a rapid melting-and-cooling process whose cooling could reach to ~ 10^6

K/s[23]. And during the fusing, the maximum temperature in the melting pool could also reach to 4000K in the argon atmosphere[24]. The solidification texture is determined by local temperature and competitive grain growth at the liquid-solid interface [25]. The temperature of the melting pool can be influenced by LPBF parameters such as laser power, laser spot size, scanning strategy, layer thickness, etc. As reported by Higashi et al.[26], in additive manufactured Mo samples, crystallographic texture varied with volumetric energy density: a strong <110> fiber texture was observed at high laser powder and low scan speed(400mm/) while a <001>fiber texture dominated in the microstructure when the scan speed was increased to 800mm/s. In terms of competitive grain growth, it can also be classified as surface energy-driven preferential grain growth. In the conventional high-temperature annealing processing, the {100} texture of the electric steel corresponding to the lowest surface energy preferentially grows in vacuum or high purity inert gas[27]. According to the first principle of DFT calculation, the {100} family of planes possess the lowest surface energy, which means that grains with the (00l) orientation (in the surface-normal direction) or (h00) orientation (in the surface-parallel direction) have the lowest surface energy thereby growing more faster than other crystallographic directions[28]. According to the Vito`s full charge density (FCD) calculation[29], the surface energy of Fe(100)&Fe(110) are 2.22J/m^2 and 2.43J/m^2 while this value of Fe(111) is 2.733J/m^2. This may explain why there are strong (100) fiber textures and (110) fiber textures on the X&Z plane of additively manufactured FeSi alloy. Fig. 9 illustrates the process of LPBF and the crystallographic orientation inside the additive manufactured FeSi bulk samples. Combing with the ODF data and IPF mappings, there are {001} and {110} grains consisting of the FeSi alloy. And the deviation angle between the Z-axis and the grain abnormal axis is within 20°.

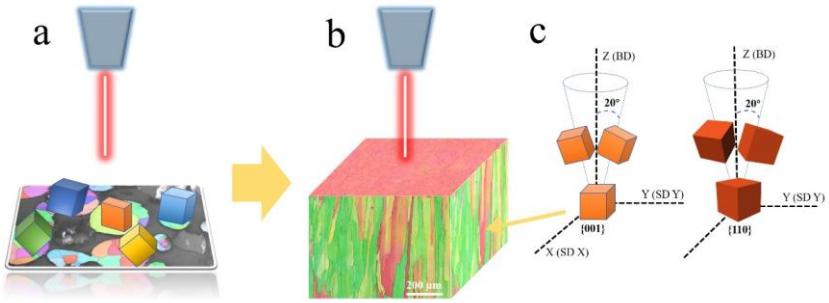

Fig. 9 The schematic diagram of LPBF process and texture distribution (a) before LPBF; (b) after LPBF;(c) crystallographic orientation in the additive manufacture FeSi alloy.

5. Summary

In this work, the texture and microstructure of additively manufactured Fe-3.5wt% alloy were investigated. The conclusions are summarised as follows:

1) A strong λ-fiber//ND texture was observed on the top plane of additively manufactured Fe-3.5% alloy.
2) There is almost no Goss texture on the top plane of LPBF Fe-3.5 wt% alloy.

3) Rotated Cube texture was obtained on the top plane of LPBF Fe-3.5 wt% alloy.

4) A Si&O-rich amorphous precipitate was formed in the Fe-3.5wt% alloy after LPBF processing.

Our findings illustrated that LPBF can be used to manufacture grain-oriented electric steel. In terms of the effects of amorphous precipitates, more detailed investigations will be carried out.

Declaration of Competing Interest

The authors declare that they have not known competing for financial interests or personal relationships that could have influenced the work report in this paper.

Acknowledgments

We would like to acknowledge the Facility for Analysis, Characterisation, Testing and Simulation, Nanyang Technological University, Singapore, for use of their facilities. The work was supported by National Research Foundation (NRF) Singapore under its NRF Fellowship Grant NRF- NRFF12-2020-0003 and the Individual Research Grant (Grant reference No.: A20E7c0109) of the Agency for Science, Technology and Research of Singapore.

Data availability

The raw/processed data required to reproduce these findings cannot be shared at this time as the data is a part of an ongoing project.

Reference

[1] A. Krings, A. Boglietti, A. Cavagnino, S. Sprague, Soft Magnetic Material Status and Trends in Electric Machines, IEEE Trans. Ind. Electron., 64 (2017) 2405-2414.

[2] J. Qin, Y. Yue, Y. Zhang, Y. Cao, P. Yang, Comparison between strong η-fiber-oriented high-silicon steel and grain-oriented high-silicon steel on magnetic properties, J. Magn. Magn. Mater., 439 (2017) 38-43.

[3] S. Takajo, C.C. Merriman, S.C. Vogel, D.P. Field, In-situ EBSD study on the cube texture evolution in 3 wt% Si steel complemented by ex-situ EBSD experiment — From nucleation to grain growth, Acta Mater., 166 (2019) 100-112.

[4] S. Taguchi, A. Sakakura, The effects of AlN on secondary recrystallization textures in cold rolled and annealed (001)[100] single crystals of 3% silicon iron, Acta Metall. Mater., 14 (1966) 405-423.

[5] T. Tomida, T. Tanaka, Development of (100) texture in silicon steel sheets by removal of manganese and decarburization, ISIJ Int., 35 (1995) 548-556.

[6] H.-T. Liu, Z.-Y. Liu, Y. Sun, Y.-Q. Qiu, C.-G. Li, G.-M. Cao, B.-D. Hong, S.-H. Kim, G.-D. Wang, Formation of {001} <510> recrystallization texture and magnetic property in strip casting non-oriented electrical steel, Mater. Lett., 81 (2012) 65-68.

[7] F. Fang, Y.X. Zhang, X. Lu, Y. Wang, M.F. Lan, G. Yuan, R.D.K. Misra, G.D. Wang, Abnormal growth of {100} grains and strong Cube texture in strip cast Fe-Si electrical steel, Scr. Mater., 147 (2018) 33-36.

[8] M. Mehdi, Y. He, E.J. Hilinski, L.A.I. Kestens, A. Edrisy, The evolution of cube ({001}<100>) texture in non-oriented electrical steel, Acta Mater., 185 (2020) 540-554.

[9] M. Zhou, X. Zhang, Regulating the recrystallized grain to induce strong cube texture in oriented silicon steel, J Mater Sci Technol, 96 (2022) 126-139.
[10] M. Garibaldi, I. Ashcroft, M. Simonelli, R. Hague, Metallurgy of high-silicon steel parts produced using Selective Laser Melting, Acta Mater., 110 (2016) 207-216.
[11] M. Garibaldi, I. Ashcroft, J.N. Lemke, M. Simonelli, R. Hague, Effect of annealing on the microstructure and magnetic properties of soft magnetic Fe-Si produced via laser additive manufacturing, Scr. Mater., 142 (2018) 121-125.
[12] D. Goll, D. Schuller, G. Martinek, T. Kunert, J. Schurr, C. Sinz, T. Schubert, T. Bernthaler, H. Riegel, G. Schneider, Additive manufacturing of soft magnetic materials and components, Addit. Manuf., 27 (2019) 428-439.
[13] A. Plotkowski, K. Carver, F. List, J. Pries, Z. Li, A.M. Rossy, D. Leonard, Design and performance of an additively manufactured high-Si transformer core, Materials & Design, 194 (2020).
[14] B. Koo, M.-S. Jang, Y.G. Nam, S. Yang, J. Yu, Y.H. Park, J.W. Jeong, Structurally-layered soft magnetic Fe-Si components with surface insulation prepared by shell-shaping selective laser melting, Appl. Surf. Sci., 553 (2021).
[15] G.S. Kumar, M. Sateshwar, A.R. Sharma, M. Palit, R. Sarkar, P. Ghosal, G.A. Rao, Particle size dependent microstructure evolution of inert gas atomized nickel base superalloy powders, J. Alloys Compd., 909 (2022).
[16] A. Plotkowski, J. Pries, F. List, P. Nandwana, B. Stump, K. Carver, R.R. Dehoff, Influence of scan pattern and geometry on the microstructure and soft-magnetic performance of additively manufactured Fe-Si, Addit. Manuf., 29 (2019).
[17] N. Shayesteh Moghaddam, S. Saedi, A. Amerinatanzi, A. Hinojos, A. Ramazani, J. Kundin, M.J. Mills, H. Karaca, M. Elahinia, Achieving superelasticity in additively manufactured NiTi in compression without post-process heat treatment, Sci Rep, 9 (2019) 41.
[18] S. Wei, K.B. Lau, J.J. Lee, F. Wei, W.H. Teh, B. Zhang, C.C. Tan, P. Wang, U. Ramamurty, Selective laser melting of Fe–Al alloys with simultaneous gradients in composition and microstructure, Mater. Sci. Eng. A, 821 (2021).
[19] I. Ferretto, D. Kim, N.M. Della Ventura, M. Shahverdi, W. Lee, C. Leinenbach, Laser powder bed fusion of a Fe–Mn–Si shape memory alloy, Addit. Manuf., 46 (2021).
[20] S. Takajo, S.C. Vogel, Y. Hayakawa, Strongly Developed Texture Components near Rotated Cube Orientation during Recrystallization in a Severely Cold Rolled Low Carbon Steel, ISIJ Int., 59 (2019) 541-550.
[21] S.K. Chang, S.I. Lee, D.N. Lee, Change of Rotated Cube Texture through Multi-processing in 3% Si-steels, ISIJ Int., 49 (2009) 105-108.
[22] A. Zafari, K. Xia, Laser powder bed fusion of ultrahigh strength Fe-Cu alloys using elemental powders, Addit. Manuf., 47 (2021).
[23] U. Scipioni Bertoli, G. Guss, S. Wu, M.J. Matthews, J.M. Schoenung, In-situ characterization of laser-powder interaction and cooling rates through high-speed imaging of powder bed fusion additive manufacturing, Materials & Design, 135 (2017) 385-396.
[24] P.A. Hooper, Melt pool temperature and cooling rates in laser powder bed fusion, Addit. Manuf., 22 (2018) 548-559.
[25] H.L. Wei, J. Mazumder, T. DebRoy, Evolution of solidification texture during additive manufacturing, Sci Rep, 5 (2015) 16446.
[26] M. Higashi, T. Ozaki, Selective laser melting of pure molybdenum: Evolution of defect and

crystallographic texture with process parameters, Materials & Design, 191 (2020).
[27] F. Assmus, K. Detert, G. Ibe, Über eisen-silizium mit würfeltextur, Int. J. Mater. Res., 48 (1957) 344-349.
[28] J. Moon, S. Kwon, M. Alahbakhshi, Y. Lee, K. Cho, A. Zakhidov, M.J. Kim, Q. Gu, Surface Energy-Driven Preferential Grain Growth of Metal Halide Perovskites: Effects of Nanoimprint Lithography Beyond Direct Patterning, ACS Appl. Mater. Interfaces, 13 (2021) 5368-5378.
[29] L. Vitos, A.V. Ruban, H.L. Skriver, J. Kollár, The surface energy of metals, Surf. Sci., 411 (1998) 186-202.